Nanoscale

PAPER

View Article Online
View Journal | View Issue

Cite this: *Nanoscale*, 2020, **12**, 14076

Unraveling the mechanism of the one-pot synthesis of exchange coupled Co-based nano-heterostructures with a high energy product†

Beatrice Muzzi, [a,b,c] Martin Albino, [c] Claudia Innocenti, [b,c] Michele Petrecca, *[b,c] Brunetto Cortigiani, [c] César de Julián Fernández, [d] Giovanni Bertoni, [d,e] Rodrigo Fernandez-Pacheco, [f,g,h] Alfonso Ibarra, [f,g,h] Clara Marquina, [i,f] M. Ricardo Ibarra [i,f,g,h] and Claudio Sangregorio *[b,c]

The development of reproducible protocols to synthesize hard/soft nano-heterostructures (NHSs) with tailored magnetic properties is a crucial step to define their potential application in a variety of technological areas. Thermal decomposition has proved to be an effective tool to prepare such systems, but it has been scarcely used so far for the synthesis of Co-based metal/ferrite NHSs, despite their intriguing physical properties. We found a new approach to prepare this kind of nanomaterial based on a simple one-pot thermal decomposition reaction of metal-oleate precursors in the high boiling solvent docosane. The obtained NHSs are characterized by the coexistence of Co metal and Co doped magnetite and are highly stable in an air atmosphere, thanks to the passivation of the metal with a very thin oxide layer. The investigation of the influence of the metal precursor composition (a mixed iron–cobalt oleate), of the ligands (oleic acid and sodium oleate) and of the reaction time on the chemical and structural characteristics of the final product, allowed us to rationalize the reaction pathway and to determine the role of each parameter. In particular, the use of sodium oleate is crucial to obtain a metal phase in the NHSs. In such a way, the one-pot approach proposed here allows the fine control of the synthesis, leading to the formation of stable, high performant, metal/ferrite NHSs with tailored magnetic properties. For instance, the room temperature maximum energy product was increased up to 19 kJ m^{-3} by tuning the Co content in the metal precursor.

Received 17th February 2020,
Accepted 3rd June 2020

DOI: 10.1039/d0nr01361g

rsc.li/nanoscale

1. Introduction

The capability of shaping matter to create complex hybrid nanoarchitectures has represented a major step forwards in nanoscience to develop innovative and multifunctional materials. Combining components at the nanoscale endowed with different physical properties, either strongly interacting or not, can indeed largely expand and enhance the material functionalities, and, in some cases, enable the emergence of new properties. The resulting multifunctional nanomaterials are then promising candidates to address many of the challenges of the next future in a wealth of research areas, ranging from biomedicine to electronics. In this regard, magnetic hybrid nanostructures are particularly promising. Coupling at the nanoscale materials with intrinsically different magnetic properties, indeed, allows the observation of novel magnetic phenomena, the most prominent being exchange bias and exchange spring coupling. The former originates from the exchange interactions between differently ordered magnetic phases, usually an antiferromagnet and a ferro- or ferrimag-

[a]*Dept. of Biotechnology, Chemistry and Pharmacy, University of Siena 1240, I-53100 Siena, Italy*
[b]*ICCOM – CNR, I-50019 Sesto Fiorentino (FI), Italy.*
E-mail: petrecca.michele@gmail.com, csangregorio@iccom.cnr.it
[c]*Dept. of Chemistry "U. Schiff", University of Florence and INSTM, I-50019 Sesto Fiorentino (FI), Italy*
[d]*IMEM – CNR, I-43124 Parma, Italy*
[e]*CNR – Istituto Nanoscienze, I-41125 Modena, Italy*
[f]*Dpto. de Física de la Materia Condensada, Universidad de Zaragoza, 50009-Zaragoza, Spain*
[g]*Instituto de Nanociencia de Aragón (INA), Universidad de Zaragoza, 50018-Zaragoza, Spain*
[h]*Laboratorio de Microscopias Avanzadas (LMA), Universidad de Zaragoza, 50018-Zaragoza, Spain*
[i]*Instituto de Ciencia de Materiales de Aragón (ICMA), Consejo Superior de Investigaciones Científicas (CSIC)-Universidad de Zaragoza, 50009-Zaragoza, Spain*

†Electronic supplementary information (ESI) available: TEM images; XPS spectra; EELS elemental and quantification analysis; magnetic measurements; all experimental details about the synthesis performed to study the synthetic protocol; XRD patterns. See DOI: 10.1039/d0nr01361g

netic one,[1] while the second is obtained by combining at the nanoscale a high anisotropy hard magnetic phase with a high magnetization soft magnetic phase.[2]

These phenomena have been proposed in the recent past as efficient strategies to enhance the performances of permanent magnets (PM).[3–5] PMs are key elements of many technological devices used in everyday life,[6] such as hard disks, automotive devices, wind turbines, electronic components, and hybrid electric vehicles. Their performance is quantified by the so-called maximum energy product, BH_{max}, which describes the maximum amount of magnetic energy storable in a magnet.[7] By far, the most powerful magnets comprise rare earth (RE) elements. However, the criticality about the sustainability of the RE chain supply that emerged in the last decade[8] has brought about renewed interest towards novel RE-free materials which can provide a viable alternative to RE, at least in all those applications where large performances are not strictly required.[9]

Among the various strategies investigated to date, considerable interest has been directed towards exchange coupled hard/soft nano-heterostructures (NHSs). The $M/Co_xFe_{3-x}O_4$ nanosystem, where M is Fe, Co or a Co–Fe alloy, is indeed one of the best materials to investigate the feasibility of this approach, as it comprises a soft metal with the highest saturation magnetization, M_S, ($CoFe_2$ has M_S = 245 A m^2 kg^{-1}),[10] and a hard ferrite ($Co_xFe_{3-x}O_4$ has magnetic anisotropy up to 10^6 J m^{-3} and a magnetization of 88 A m^2 kg^{-1} for $x = 0.6$);[11–13] moreover, it offers the opportunity to convert one phase into the other by a simple oxidation/reduction process. Nevertheless, although simple in principle, the practical realization of high quality Co-based NHSs is a rather complex task. On the one hand, in fact, the synthesis of stable metal cobalt or cobalt–iron cores by microemulsion[14] or thermal decomposition of $Co_2(CO)_8$ [15] and metal acetylacetonate is already well established.[16] However, on the other hand, the following reduction/oxidation step required to obtain exchange coupled NHSs often leads to low crystallinity materials with not well-defined and partially disordered interfaces. Consequently, the resulting products are characterized by low saturation magnetization, small remanence and/or weak magnetic coupling.[17–20] On the other hand, thermal decomposition of metal–organic precursors has proved to be effective for producing Fe/Fe_3O_4 core–shell NPs with well-defined architectures, high quality interfaces and good magnetic properties.[21] However, to our knowledge, the technique has been scarcely extended to the synthesis of Co-analogous heterostructures, $Co/Co_xFe_{3-x}O_4$. This is rather surprising since Co-based NHSs are extremely appealing for several applications, particularly when materials combining large hysteresis loops and high magnetization are required.[11] The replacement of $Fe^{(II)}$ ions in octahedral sites with the high anisotropy $Co^{(II)}$ ones, indeed, largely increases the magnetic anisotropy of the spinel ferrites without compromising the M_S.[13] For this reason, cobalt ferrite has been proposed for application in electronics, biomedicine, catalysis and as building blocks for the realization of rare earth free permanent magnets.[11,22–26]

Despite the large experimental work carried out in the last 20 years, the synthesis of magnetic NPs by thermal decomposition is still far from being fully rationalized. Indeed, a very large number of parameters concur to determine the nature of the final product,[27,28] making the unambiguous identification of their role a complex task. As a result, the synthesis by this technique of Co-based NHSs with pre-determined architecture and composition is still challenging.

Here, we report an experimental investigation on the use of one pot thermal decomposition of mixed iron–cobalt oleate in a high boiling organic solvent, (docosane) to prepare Co/spinel ferrite NHSs with high crystallinity and a controlled composition. In particular, the influence of ligands, metal precursors and reaction time was carefully investigated. The study allowed us to propose a reaction mechanism where sodium oleate plays a crucial role in the formation of a metal cobalt phase. In this way, we were able to identify the key parameters controlling the reaction pathway, paving the way towards the rational design of Co-based NHSs with controlled magnetic properties.

2. Experimental

2.1 Chemicals and materials

Iron(III) chloride hexahydrate ($FeCl_3{\cdot}6H_2O$, 98% from Sigma-Aldrich), cobalt(II) chloride hexahydrate ($CoCl_2{\cdot}6H_2O$, 98% from Honeywell), sodium oleate (NaOL, >97%, TCI Chemicals), oleic acid (OA, 90%, Aldrich), docosane (97%, Aldrich), ethanol (99.8%, Fluka), hexane (99%, Honeywell) and 2-propanol (98%, Honeywell) were used without any further purification.

2.2 Synthesis of the iron–cobalt oleate (*x*-FeCo(OL)) precursor

Bimetal oleate precursors, *x*-FeCo(OL), with a Fe : Co molar ratio of 2 : 1 (1-FeCo(OL)), 1 : 1 (2-FeCo(OL)) and 1 : 2 (3-FeCo (OL)) were synthesized by dissolving the desired stoichiometric amount of $FeCl_3{\cdot}6H_2O$ and $CoCl_2{\cdot}6H_2O$ in 20 mL of hexane, 10 mL of ethanol and 10 mL of distilled water. At room temperature, a stoichiometric amount of NaOL was added and the mixture was heated at 75 °C, under vigorous stirring, for 5 hours. The brown colored organic phase was separated from the aqueous phase and a brown-dark waxy product was obtained after solvent evaporation. The stoichiometry of the final product was confirmed by Inductively Coupled Plasma analysis. The thermal stability of the ligand was studied by thermogravimetric analysis, (TGA) using Q-600 (DTA-TG) apparatus with open aluminum pans under a nitrogen atmosphere.

2.3 Synthesis of $Co/Co_yFe_{3-y}O_4$ NPs

The $Co/Co_yFe_{3-y}O_4$ NPs were synthesized by thermal decomposition of the bimetallic precursor. 1.5 g (*ca.* 2 mmol of metal ions) of *x*-FeCo(OL), 0.57 g (2 mmol) of OA and 0.57 g (1.8 mmol) of NaOL were dissolved in 10 mL of docosane at 80 °C. The mixture was heated from 80 to 370 °C, at 2.9 °C

min^{-1}, under vigorous stirring and nitrogen flux. The suspension was kept at 370 °C for 40 minutes and then allowed to cool to room temperature. The resulting black powder was separated by application of an external magnet, washed with 2-propanol, hexane and ethanol and finally dried under nitrogen flux.

2.4 Characterization techniques

Transmission electron microscopy (TEM, CM12 Philips equipped with a LaB_6 filament operating at 100 kV) was employed to determine morphology and size distribution of the NPs. The mean diameter and the NP size distribution for each sample were obtained by statistical analysis over more than 100 NPs, using Image Pro-Plus software. Powder X-Ray diffraction (XRD) data were recorded using a Bruker New D8 ADVANCE ECO diffractometer equipped with a Cu Kα (1.5406 Å) radiation source and operating in θ–θ Bragg–Brentano geometry at 40 kV and 40 mA. The measurements were carried out in the range of 25–70°, with a step size of 0.03° and a collection time of 1 s. Elemental analysis was performed in triplicate using a PerkinElmer Optima 2000 PerkinElmer Inductively Coupled Plasma Optical Emission Spectrophotometer (ICP-OES) Dual Vision. The amount of organic ligand on the surface of NHSs was determined by CHN analysis with an Elemental Analyzer CHN-S Flash E1112 Thermofinnigan. X-ray Photoelectron Spectroscopy (XPS) investigation was carried out using a non-monochromatic X-ray source (V.S.W. Scientific Instrument Limited model TA10, Mg Kα radiation, 1253.6 eV), operating at 12 kV and 12 mA, equipped with a hemispherical analyser (V.S.W. Scientific Instrument Limited, model HA100). Powders were deposited on a KBr disk and pressed to obtain a single pellet. XPS spectra were analyzed with CasaXPS software: the inelastic background was subtracted by means of the Shirley method[29] and the deconvolution of the XPS spectra was carried out using the product of Gaussian and Lorentzian line shapes for each component in the spectra. Calibration was performed using the O 1s peak at 530.0 eV. Scanning transmission electron microscopy (STEM) images were acquired on a probe-corrected Titan (Thermo Fischer Scientific), with a working voltage of 300 kV. The microscope was equipped with a high annular dark field (HAADF) detector for imaging (Fischione) and an energy filter Gatan Tridiem 866 ERS (Gatan, Inc.) for Electron Energy Loss Spectroscopy (EELS) mapping. The EELS elemental maps were obtained by fitting the (x, y, E) spectrum images by the model based technique,[30] to extract the intensity of the O-K edge (at ~532 eV), the Fe-$L_{2,3}$ edge (at ~710 eV) and Co-$L_{2,3}$ edge (at ~780 eV). The spectrum images were acquired with probe convergence semi-angle α = 24.8 mrad and spectrometer collection angle semi-angle β = 51.3 mrad. See the ESI† for details on the quantification procedure. In order to obtain the crystalline structure of the different phases present in the system, an image-corrected Titan3 (Thermo Fischer Scientific) ultra-high resolution electron transmission microscope (UHRTEM) was operated at 300 kV. Magnetic properties were investigated using a Quantum Design MPMS SQUID magnetometer on randomly oriented pressed powder pellets. The field was always applied parallel to the pellet plane. The Zero Field Cooled/Field Cooled (ZFC/FC) procedure was performed applying a 5 mT probe field.

3. Results and discussion

Metal/ferrite NHSs were prepared by thermal decomposition of 2 : 1 mixed iron–cobalt oleate (1-FeCo(OL)) in the high boiling solvent docosane (T_{eb} = 368.7 °C) in the presence of sodium oleate and oleic acid. Fig. 1, left panel, shows a STEM image of sample NHS-1 and the corresponding size distribution. The sample consists of polydisperse NPs coated with *ca.* 4% w/w of oleate surfactant, as evaluated by CHN Analysis, with an irregular shape and an average diameter, estimated from the largest dimension measured on each NP, of *ca.* 90 ± 12 nm.

The XRD pattern (Fig. 1, right panel) indicates that different crystallographic phases occur in the nanopowder. Indeed, the peaks characteristic of the partially inverse spinel structure of cobalt doped ferrite (black reference), hexagonal and face-centered-cubic metal cobalt (red and blue references) can be recognized. The peak at 2θ = 45.1 degrees can be indexed as arising from the diffraction plane (110) of the cobalt–iron alloy (green reference). The Rietveld analysis of the experimental pattern, detailed in Table 1, showed for the ***Fd$\bar{3}$m*** structure of $Co_yFe_{3-y}O_4$ NPs an average crystal size of 41(1) nm, with a lattice parameter a = 0.8397(1) nm. The metal cobalt crystallized in the cubic (space group ***Fm$\bar{3}$m***) and hexagonal (space group ***P63/mmc***) structures, with an average crystallite size of 17(1) nm and 5(1) nm, respectively, while the $Co_{1-x}Fe_x$ alloy grains (cubic structure, ***Im$\bar{3}$m***) have an average size of 12(1) nm and a = 0.2847(1) nm, which is consistent with a Co : Fe ratio of *ca.* 1 : 1. The weight percentages of the three crystallographic structures are 77(2)% for the ferrite, 13(2)% for the metal Co (mostly *fcc* with traces of *hcp*) and 10(2)% for the alloy.

Further information about the chemical composition of the magnetic phases was obtained by XPS measurements. Since the technique is surface sensitive, the NHS-1 powder was pressed on top of a pre-consolidated KBr pellet and then sub-

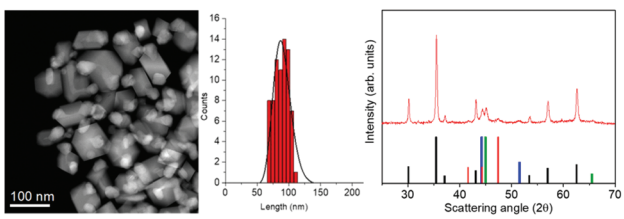

Fig. 1 (Left) A representative STEM image of NHS-1 NPs and the corresponding size distribution as evaluated from TEM analysis (see also Fig. S1 in the ESI†); (right) experimental XRD pattern (red line) and reference patterns of: $CoFe_2O_4$, (JCPDS PDF #22-1086); *hcp* $Co^{(0)}$ (JCPDS PDF #89-7373); *fcc* $Co^{(0)}$, (JCPDS PDF #15-0806), and Co–Fe alloy, (JCPDS PDF #65-4131).

Table 1 Lattice parameters (*a* and *c*), average crystallite size (*D*) and phase percentage obtained from Rietveld refinement of XRD patterns and from the deconvolution of Co and Fe XPS peaks of NHS-1

	XRD			XPS
NHS-1	Lattice parameters (nm)	Crystal size (*D*) (nm)	Phase percentage (%)	Phase percentage (%)
Co (*fcc*)	a = 0.3546(1)	17(1)	11(2)	19(5)
Co (*hcp*)	a = 0.2507(1) c = 0.4085(1)	5(1)	2(1)	
Co–Fe alloy	a = 0.2847(1)	12(1)	10(2)	
$Co_yFe_{3-y}O_4$	a = 0.8397(1)	41(1)	77(2)	81(5)

jected to a series of ion beam etching and spectrum acquisition cycles (removal of *ca.* 5 nm thickness per cycle) until a constant spectrum profile was obtained (see Fig. S2, ESI†). Once this condition is reached, the collected signal becomes representative of the whole sample, independent of the element distance from the NP surface. Fig. 2 reports the XPS spectra in the Co and Fe threshold energy regions. The deconvolution of the Co $2p_{3/2}$ peak (Fig. 2, left panel) revealed the presence of three components, which can be attributed to $Co^{(0)}$ metal (red peak at 778.2 eV)[31] and to $Co^{(II)}$ in octahedral (*Oh*) and tetrahedral (*Td*) sites of the non-stoichiometric $Co_yFe_{3-y}O_4$ (blue and green peaks at 780 and 782.4 eV, respectively)[32] and, at higher binding energy, a satellite peak (light blue one at 784.7 eV). The Fe $2p_{3/2}$ peak (Fig. 2, right panel) was successfully deconvoluted by five components: the lowest binding energy component at 706.7 eV (purple peak) was attributed to $Fe^{(0)}$,[31] while the three components at 708.9 eV (green), 710.7 eV (blue) and 712.7 eV (red) were ascribed to octahedral $Fe^{(II)}$/$Fe^{(III)}$ and tetrahedral $Fe^{(III)}$, respectively.[31] The satellite peaks related to $Fe^{(II)}$ and $Fe^{(III)}$ were resolved as a single peak at 715.3 eV (light blue).[33,34]

The quantitative analysis of these signals, summarized in Table 1, indicated the formation of 19(5)% of metal phase (11% of $Co^{(0)}$ and 8% of $Fe^{(0)}$) and 81(5)% of a spinel ferrite

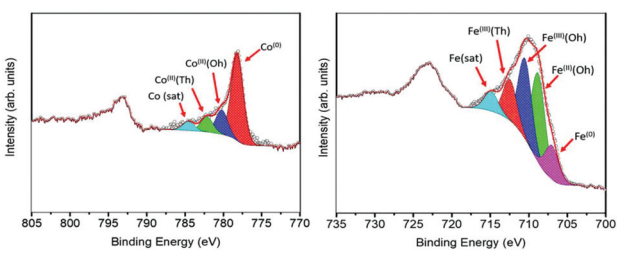

Fig. 2 XPS spectra of NHS-1 in the region of cobalt (left) and iron (right). Spectra were recorded after four Ar ion beam etching cycles (removing *ca.* 5 nm thickness per cycle). The Co $2p_{3/2}$ peak was fitted with four components: $Co^{(0)}$ metal (red peak), $Co^{(II)}$ in octahedral (*Oh*) and tetrahedral (*Td*) sites of the $Co_yFe_{3-y}O_4$ (blue and green, respectively) and a satellite peak (cyan). The Fe $2p_{3/2}$ peak was deconvoluted by five components: $Fe^{(0)}$ metal (purple), octahedral $Fe^{(II)}$ (green) and $Fe^{(III)}$, (blue), tetrahedral $Fe^{(III)}$ (red), and a satellite peak (cyan).

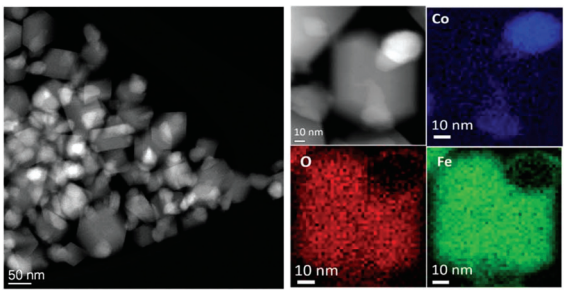

Fig. 3 (Left) STEM image of NHS-1 NPs; (right) EELS mapping of NHS-1 and distributions inside one NP of oxygen (O-K edge, red), iron (Fe-$L_{2,3}$ edge, green) and cobalt (Co-$L_{2,3}$ edge, blue).

doped with a very low content of cobalt, according to the results obtained by Rietveld analysis of the XRD pattern.

With the aim to understand the structure of the synthesized sample, the element distribution was examined through the STEM-EELS technique. The STEM image of a single NP (Fig. 3, left panel) showed the presence of well-defined areas with higher brightness, probably corresponding to $Co^{(0)}$ and the Co–Fe alloy, and regions with lower brightness, corresponding to the metal oxide. The STEM-EELS mapping confirmed this hypothesis, depicting an overlapped distribution of oxygen and iron (Fig. 3, right panel) in the darker areas, while cobalt was inhomogeneously distributed, with a much higher percentage in the bright areas of the STEM image. From EELS measurements, it was harder to discriminate the presence of metallic $Fe^{(0)}$ due to the high amount of Fe from both the spinel ferrite phase and the oxide shell.

STEM images and EELS data therefore indicated that the NPs can be described as heterodimers comprising iron and cobalt in the metal state and a Co-poor spinel ferrite. Moreover, they suggested that the metal is covered by a very thin metal oxide layer (*ca.* 3 nm), whose presence justifies the long-time stability of the NPs. This was confirmed by an in-depth STEM-EELS analysis of the metal Co surface (Fig. 4 and Fig. S4 in the ESI†).

The sub-nm resolved EELS mapping performed on a 5 nm thick layer of the NHS-1 NP surface highlighted the chemical composition of the shell. In the most external part of the shell (region 1), *ca.* 1 nm of thickness, the percentage of iron and cobalt was 60(6)% and 40(4)%, respectively. Moving deeper inside the NP, the amount of iron decreased progressively until it was no more detected close to the metal core (region 6). Thus, we can conclude that the oxide surrounding the metal is a quasi-stoichiometric cobalt ferrite. The other phase has a composition close to that of magnetite, with a very low amount (y < of 0.04) of cobalt.

In order to better understand the crystalline structure of the NHS, HRTEM images were acquired and their local Fast Fourier Transformation (FFT) was analyzed. In Fig. 5I, the image of a NP of NHS-1 is shown as representative of the whole powder sample. Two parts with spherical and cubic morphology can be distinguished. The corresponding magnifi-

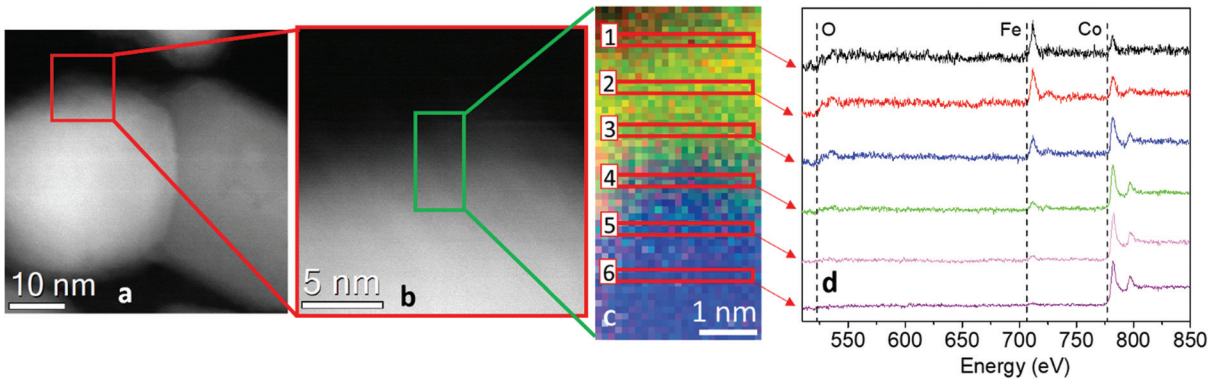

Fig. 4 (a) STEM image of NHS-1 NP and (b) magnification of the shell region (5 nm thickness) from the red square in (a). (c) EELS color mapping of the selected green region (*ca.* 3 × 6 nm) in b panel; this area was chosen as representative of the shell at the metal surface, where the blue and green spots refer to cobalt and iron, respectively. (d) Normalized EELS spectra related to the regions in the EELS color map. The peaks at 708 eV and 779 eV correspond to the $L_{2,3}$ edge of iron and of cobalt, respectively. In the outer surface (region 1 in c), it is possible to distinguish both iron and cobalt edges (intensity 60(6)% and 40(4)%, respectively). Moving towards the inner side (regions 2–6), the iron signal decreases until it disappears (region 6).

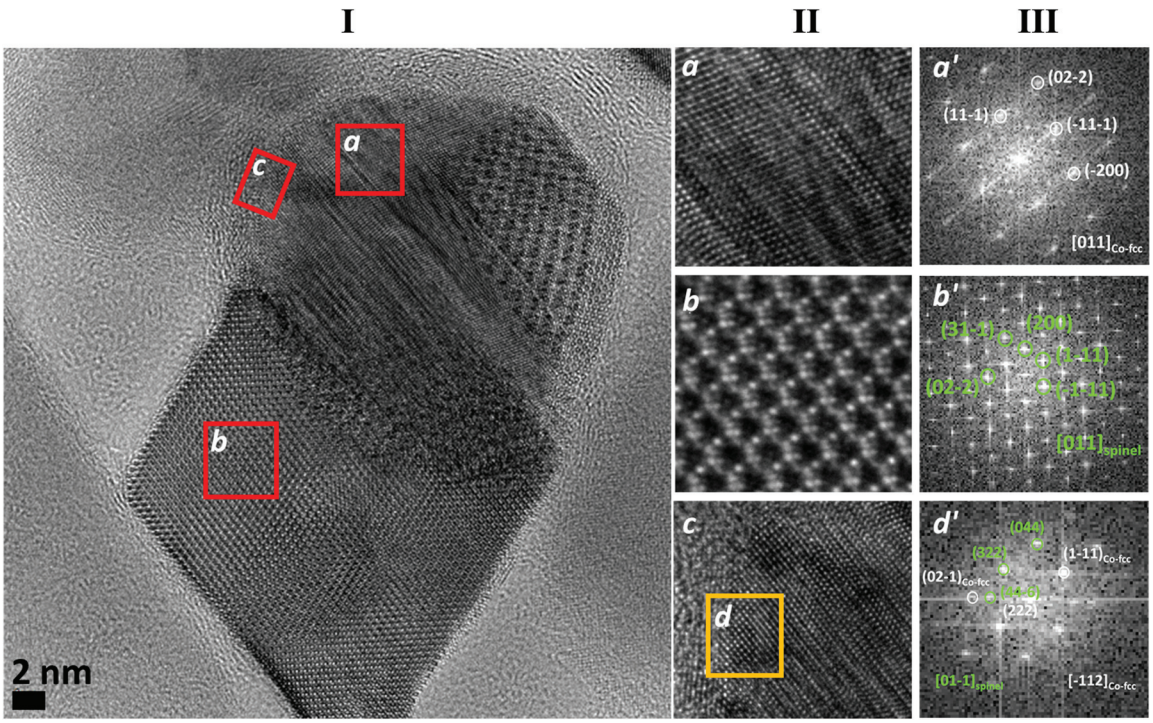

Fig. 5 (I) HRTEM image of a NHS-1 NP, where 3 regions (a–c) are selected: a and b correspond to metal and ferrite cores, respectively, while the region c to the shell around the metal core; (II) enlargement of the selected regions in I; (III) FFT analysis of the regions a, b, and d (yellow square in c) showing the presence of different crystallographic structures: the labelled spots are related to crystallographic planes that can be indexed as: (a′) *fcc* metal phase ($Fm\bar{3}m$), in zone axis $[011]_{Co\text{-}fcc}$, (b′) cubic spinel structure ($Fd\bar{3}m$), $[011]_{spinel}$ and (d′) metal (white) and cubic spinel oxide (green) phases, $[01\text{–}1]_{spinel}$ and $[\text{–}112]_{Co\text{-}fcc}$; the presence of both phases confirms a sharp interface.

cations (a and b, respectively), together with the one related to the outer shell of the spherical part (c), are shown in Fig. 5II. The FFT analysis, performed on a and b, revealed the presence of the *fcc*-structure of metal cobalt (Fig. 5III-a′) and of the cubic spinel structure of $Co_yFe_{3-y}O_4$ (Fig. 5III-b′). The FFT performed on the selected region of the outer metal shell (d in Fig. 5II-c) showed the coexistence of spots related to both the *fcc* cobalt and the spinel ferrite (Fig. 5III-d′), confirming the presence of an interface between the two phases. Altogether this information indicated that NHS-1 comprises two components, a faceted spinel ferrite and a metal core, the latter being surrounded by a highly crystalline, thin ferrite layer.

The magnetic properties of NHS-1 were first investigated by the measurement of the hysteresis loops at 5 K and 300 K (Fig. 6, left panel). In both loops, a single step magnetization reversal process was observed, as generally expected for strongly exchange coupled magnetic phases. The M_S values at 300 K and 5 K, extrapolated from the high field data, were 114 A m^2 kg^{-1} and 116 A m^2 kg^{-1}, respectively. The remanence, M_R, increased from 43 A m^2 kg^{-1} up to 66 A m^2 kg^{-1} and the coercive field from 0.04 T to 0.16 T when decreasing temperature from 300 K to 5 K.

The temperature dependence of the magnetization (Fig. 6, right panel) measured after ZFC and FC procedures displayed magnetic irreversibility up to the largest investigated temperature (340 K). Interestingly, no traces of any magnetic ordering transition appear in the ZFC and FC magnetization curves, confirming the absence of antiferromagnetic species such as iron or cobalt monoxides. A kink is however observed at *ca.* 120 K, which can be attributed to the Verwey transition.[35] This observation confirmed that the oxide phase is mainly magnetite with a very low percentage of $Co^{(II)}$ in the lattice. Indeed, as reported by Abellan *et al.*, the Verwey transition in $Co_yFe_{3-y}O_4$ disappears when y is larger than 0.04.[36] In our NHSs, the presence of metal phases strongly increases M_S (30% more at room temperature) and the coercive field (90% more) with respect to those of magnetite NPs (for example, 42 nm magnetite NPs exhibit M_S = 89 A m^2 kg^{-1} and $\mu_0 H_C$ = 0.021 T, at room temperature).[37] It is interesting to note that when the hysteresis loop was measured at low temperature (5 K) after a 5 T FC procedure, no evidence of exchange bias occurred. Such observation allows us to exclude the presence of any surface spin coupling effect arising from ferro-(ferri-)/antiferro-magnetic interfaces or magnetically disordered shells in our NPs.

Despite the relatively large remanence value, the NPs in NHS-1 are still too soft to be used as building blocks for PM. In fact, the BH_{max}, evaluated after rescaling the magnetization for the volume estimated from the phase densities obtained from XPS and using the demagnetization factor ($N_{||}$ = 0.1)[38] to take into account the internal field of the pellet, was 8 kJ m^{-3}. Although the proposed synthesis method proved to be an efficient route to obtain a metal/ferrite exchange coupled nanostructure, designing a system with enhanced BH_{max}, exploitable for practical applications, requires the increase of the magnetic anisotropy of the spinel ferrite component. This can be accomplished by increasing the amount of $Co^{(II)}$ ions in the *Oh* sites of the spinel lattice. To this aim, the synthesis was repeated starting from two Co-richer mixed metal oleate complexes, 2-FeCo(OL) and 3-FeCo(OL), with a Fe : Co ratio of 1 : 1 and 1 : 2, respectively. The two precursors were prepared following the same synthetic strategy reported in the Experimental section for 1-FeCo(OL).

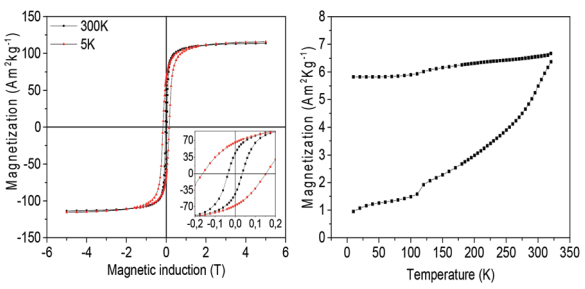

Fig. 6 (Left) Hysteresis loops of NHS-1 measured at 300 K (black) and 5 K (red); the magnification of the low field region is shown in the inset; (right) temperature dependence of the magnetization recorded after ZFC and FC procedures, applying a constant field of 5 mT.

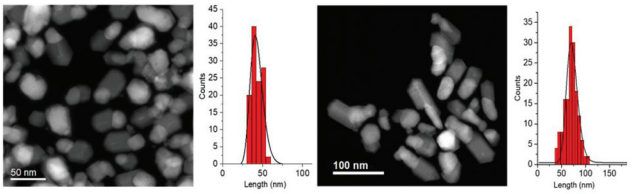

Fig. 7 STEM images and particle size distributions of NHS-2 (left) and NHS-3 (right). The size distributions are evaluated from TEM images (see Fig. S1, ESI†) considering the length of the elongation axis.

In Fig. 7 the STEM images and size distributions of the two obtained samples, NHS-2 (left) and NHS-3 (right), are shown. For both samples, it is possible to distinguish heterodimeric NPs with a mean size of about 40 ± 6 nm and 70 ± 10 nm for NHS-2 and NHS-3, respectively, and narrower size distribution compared to NHS-1 (±12 nm).

STEM images suggested that increasing the amount of cobalt in the bimetallic precursor leads to an evolution of the NPs' shape to a more elongated heterodimeric architecture. XRD patterns of both samples are shown in Fig. 8, and, similarly to that of NHS-1, they exhibit diffraction peaks corresponding to the inverse spinel structure of cobalt ferrite, and to metal cobalt and the cobalt–iron alloy.

The data obtained from the Rietveld refinement of the experimental XRD patterns are reported in Table 2. It is observed that increasing the concentration of Co in the mixed metal precursor leads to a decrease of the amount of spinel

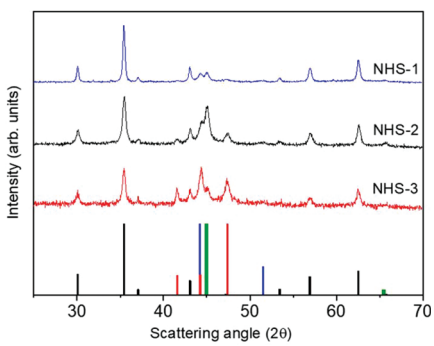

Fig. 8 XRD patterns of NHS-2 (black line) and NHS-3 (red line) NPs compared with NHS-1 (blue line). Reference bars are related to: $CoFe_2O_4$, (JCPDS PDF #22-1086); *hcp* $Co^{(0)}$ (JCPDS PDF #89-7373); *fcc* $Co^{(0)}$, (JCPDS PDF #15-0806), and Co–Fe alloy, (JCPDS PDF #65-4131).

Table 2 Lattice parameters (*a* and *c*), average crystallite size (*D*) and phase percentage obtained from Rietveld refinement of XRD patterns and from the deconvolution of Co and Fe XPS peaks for NHS-2 and NHS-3

	XRD			XPS
	Lattice parameters (nm)	Crystal size (*D*) (nm)	Phase percentage % (w/w)	Phase percentage % (w/w)
NHS-2				
Co (*fcc*)	a = 0.3541(1)	16(1)	10(2)	39(5)
Co (*hcp*)	a = 0.2510(1)	15(1)	4(2)	
	c = 0.4079(1)			
Co–Fe alloy	a = 0.2846(1)	13(1)	28(3)	
$Co_yFe_{3-y}O_4$	a = 0.8389(1)	22(1)	58(2)	61(5)
NHS-3				
Co (*fcc*)	a = 0.3541(1)	21(1)	19(2)	44(5)
Co (*hcp*)	a = 0.2506(1)	19(1)	13(2)	
	c = 0.4104(1)			
Co–Fe alloy	a = 0.2850(1)	16(1)	10(3)	
$Co_yFe_{3-y}O_4$	a = 0.8389(1)	22(1)	58(2)	56(5)

ferrite with respect to the metal phases. The weight percentages (% w/w) of the oxide and metal species were also estimated by fitting the XPS data (see Fig. S3, ESI†), obtained for both samples, following the procedure described for NHS-1. The results (Table 2) indicate the formation of 61% and 56% of Co-doped ferrite of average composition $Co_{0.3}Fe_{0.7}Fe_{2.0}O_4$ and $Co_{0.4}Fe_{0.6}Fe_{2.0}O_4$, for NHS-2 and NHS-3, respectively. The remarkable agreement between XRD and XPS data underlines the validity of the approach used to extract quantitative information of the overall composition of the NPs from a surface sensitive technique as XPS.

Therefore, increasing the amount of cobalt in the bimetallic precursor FeCo(OL) leads to a larger amount of metal species and to a Co-richer spinel ferrite. This, in turn, is expected to modify the magnetic properties of the resulting NHSs, such as the disappearance of the Verwey transition in the ZFCFC measurements due to the larger amount of Co in the spinel lattice (Fig. S5, ESI†). In Table 3, the magnetic parameters extracted from the hysteresis loops recorded at low and room temperature (Fig. S6, ESI†) are reported. The data obtained at room temperature showed an increase with respect to NHS-1 both in M_S (9% for NHS-2 and 14% for NHS-3) and in M_R (23% and 39%, respectively). Considering the bulk magnetization values of the Co–Fe alloy (M_S = 245 A m^2 kg^{-1}),[10] *fcc* and *hcp* Co, (160 A m^2 kg^{-1}),[39] magnetite (92 A m^2 kg^{-1})[7] and cobalt ferrite (80 A m^2 kg^{-1}),[12] and the weight percentage obtained from XRD measurements, average M_S = 114, 136, and 122 A m^2 kg^{-1} are estimated for NHS-1, NHS-2 and NHS-3, respectively. These values are in good agreement with the experimental ones (Table 3). The difference observed for NHS-2 and NHS-3 (*ca.* 7%) can be ascribed to variation in the alloy composition.

The increase of coercivity of NHS-2 and NHS-3 with respect to that of NHS-1 is related to the magnetic anisotropy enhancement due to the larger amount of $Co^{(II)}$ in the $Co_yFe_{3-y}O_4$ lattice and of *hcp* $Co^{(0)}$. The effective magnetic anisotropy of the hybrid NPs, indeed, is proportional to the H_CM_S product and increases along the series, doubling for NHS-3 the value of NHS-1, the one with the lowest $Co^{(II)}$ amount. The hysteresis loops display a single step magnetization reversal process, in the same way as NHS-1. This result is unexpected when theoretical predictions for spring magnets are considerded.[3] The latter suggest that in a bilayer 2D system, when the size of the soft component exceeds 2–3 times the exchange length of the hard phase, the magnetic phases are decoupled.[40,41] However, the application of this theory to NHSs has not been validated yet. Quesada *et al.*[26] investigated the magnetic properties of $CoFe_2O_4$–CoFe composites of NPs with core@shell morphology, where the size of both phases is above the exchange length and below the single domain size. The authors demonstrated that even a weak coupling between the soft and hard phases can give rise to single step loops with reduced coercivity with respect to that of the hard phase. Similarly, in the present systems, the size of all the components is below their respective single domain critical values (110 nm for *hcp* Co, 120 nm for cobalt ferrite, 70 nm for *fcc* Co, and *ca.* 50 nm for Co–Fe alloy),[7,42] and above the exchange coupling length

Table 3 Saturation magnetization, M_S, remanence, M_R (reduced remanence *R*% in brackets) and coercivity, μ_0H_C, at 5 and 300 K for NHS-1, NHS-2 and NHS-3. Maximum energy product, BH_{max}, evaluated at room temperature. The magnetic values are normalized to the weight of the inorganic component

	5 K			300 K			
Sample	M_S (A m^2 kg^{-1})	M_R (*R*%) (A m^2 kg^{-1})	μ_0H_C (T)	M_S (A m^2 kg^{-1})	M_R (*R*%) (A m^2 kg^{-1})	μ_0H_C (T)	BH_{max} (kJ m^{-3})
NHS-1	115	66 (57%)	0.16	114	43 (38%)	0.04	8
NHS-2	131	80 (61%)	0.20	127	53 (42%)	0.05	14
NHS-3	132	79 (60%)	0.20	130	60 (46%)	0.07	19

(3–5 nm). Therefore, we can hypothesize that the exchange coupling between metal phases in the core is strong, while the coupling between the core and its oxide shell is weak, giving rise anyway to a collective reversal process.

Changing the cobalt concentration in FeCo(OL) precursors, we were thus able to tune the percentage of the metal phase and the hardness of the ferrite. Accordingly, BH_{max} increased from 8 (NHS-1) up to 19 (NHS-3) kJ m^{-3}, demonstrating the effectiveness of the proposed approach in increasing the energy product. It is worth noting that this BH_{max} value is almost two times larger than those previously found for other $CoFe_2O_4/CoFe_2$ nanosystems[26,43] and among the highest reported for non-oriented rare-earth free nanostructures.[11,44] Moreover, it is comparable to the energy product of some strontium ferrite-based commercial magnets.

It is also important to stress that thanks to the passivation of the metal phase with the highly crystalline spinel oxide, which allows metal preservations, these heterodimeric systems are highly stable in the air atmosphere over a long time. After one year of exposure to air, no variation of the structural and magnetic properties was indeed observed (Fig. S8 and S9, ESI†). This feature, which is important from the point of view of application, is not trivial as Co and FeCo based nanostructures are commonly reported to be unstable upon oxidation when exposed to air for a long time.[14,16,26,45]

The chemical and structural characterization unambiguously demonstrated that the one step synthesis presented here produces NHSs comprising exchange coupled metal and spinel ferrite phases, resulting in a high remanence nanosystem. The system was obtained starting from a mixed iron cobalt precursor decomposed at high temperature in docosane, in the presence of oleic acid and sodium oleate. This points out an important difference with respect to standard synthetic approaches based on thermal decomposition of mixed iron cobalt oleate, which lead to monoxides species, or less commonly, to ferrite or complex hybrids.[46–50] Here, we succeeded in the reduction of part of the metal precursor to the metal state, and we did not observe the presence of the antiferromagnetic monoxide. We attributed these to the high amount of NaOL used in the synthesis. It is indeed well documented that NaOL plays a key role in the thermal decomposition reaction. For example, it has been reported that the presence of NaOL can induce preferential crystal growth along predetermined directions and allow the morphology control of iron oxide NPs.[51–53] The latter was justified by the influence of the cation on the interaction between the carboxylic group and the various crystallographic faces of the oxide, resulting in the control of the surface energy of the NPs. In our case, we believe that the high amount of NaOL used (the NaOL : FeCo (OL) ratio is 1 : 1) can determine, under the synthetic conditions adopted (temperature and reactant molar ratio), an increase of the reducing strength of the reaction medium, allowing the reduction of transition metal cations $Fe^{(III)}$ and $Co^{(II)}$ down to the metal state.

The fundamental role of NaOL as a reducing agent was highlighted by performing four syntheses using a variable ratio between OA and NaOL, while keeping the precursor to surfactant ratio constant (see ESI, Table S1,† for details of the synthesis). XRD patterns of the obtained samples are reported in Fig. 9 and clearly show how the formation of the metal phase critically depends on the NaOL concentration. Indeed, as expected from the literature data, the synthesis with 1-FeCo (OL) and oleic acid alone led to the formation of mixed iron–cobalt monoxide (red line). Interestingly, a pure monoxide phase was also observed when the synthesis was carried out without any kind of surfactant, *i.e.* using 1-FeCo(OL) alone (Fig. 9, black line). Increasing the NaOL to OA molar ratio to 1 : 9, it was possible to observe the growth of the spinel ferrite phase (blue line) and, for larger values (1 : 1, green line), the full disappearance of the rock salt oxide with the formation of metal phases. The synthesis carried out with only the precursor and NaOL (purple line) led to the crystallization of the ferrite and metal phases. These results showed how the presence of NaOL is fundamental for obtaining a metal phase and providing, at the same time, a simple and effective method to control the spinel ferrite to metal ratio.

It is worth noting that also the use of a mixed metal oleate precursor has an influence on the composition of the final product. Indeed, repeating the synthesis using only one monometallic precursor (Fe(OL) or Co(OL)) in the presence of OA and NaOL (molar ratio 1 : 1), the XRD pattern of the obtained NPs displayed the presence of a pure wüstite phase (FeO) when starting from Fe(OL); conversely, when pure Co(OL) was used, a mixed system comprising CoO and metal cobalt $Co^{(0)}$ was obtained (Fig. S7, ESI†). Therefore, we can conclude that both the presence of cobalt in the precursor and that of NaOL in the synthetic medium are essential for obtaining the metal species.

To better understand the formation mechanism of the metal/ferrite NHSs, we investigated the evolution of the crystallographic phases with the reaction time. To this aim, four

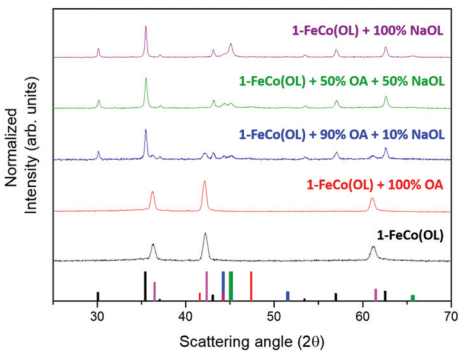

Fig. 9 XRD patterns of samples obtained using a different NaOL : OA ratio in the synthetic process: 100% OA (red line), 90% OA and 10% NaOL (blue line), 50% OA and 50% NaOL (green line) and 100% NaOL (purple line). The black bottom pattern corresponds to the powder obtained by using 1-FeCo(OL) only. Reference bars are related to: $CoFe_2O_4$, (JCPDS PDF #22-1086); CoO (JCPDS PDF #71-1178); *hcp* $Co^{(0)}$ (JCPDS PDF #89-7373); *fcc* $Co^{(0)}$, (JCPDS PDF #15-0806), and Co–Fe alloy, (JCPDS PDF #65-4131).

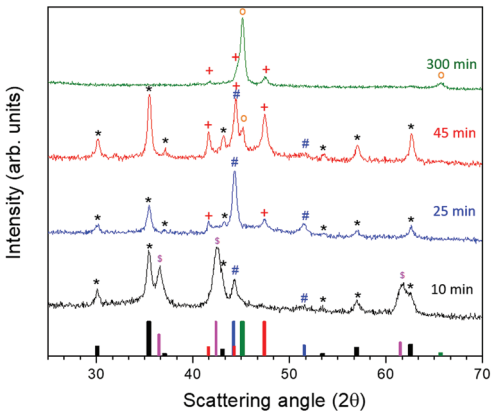

Fig. 10 XRD pattern of nanopowders prepared by increasing the reaction time: 10′ (black), 25′ (blue), 45′ (red) and 300′ (green). Reference bars are related to: $CoFe_2O_4$, (JCPDS PDF #22-1086); CoO (JCPDS PDF #71-1178); *hcp* $Co^{(0)}$ (JCPDS PDF #89-7373); *fcc* $Co^{(0)}$, (JCPDS PDF #15-0806), and Co–Fe alloy, (JCPDS PDF #65-4131). The black asterisks (*) indicate the peaks attributed to the cubic spinel structure, the magenta dollars ($) those of the monoxide phase, the blue pounds (#) of *fcc* Co, the red crosses (+) of *hcp* Co and the orange circles (o) of the cobalt–iron alloy.

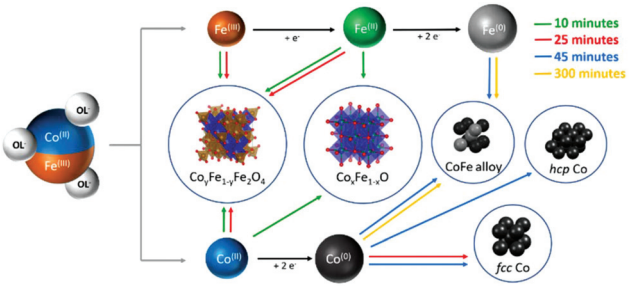

Scheme 1 Evolution of the composition of the final NHSs as a function of the dwelling time: the decomposition of the mixed Co–Fe precursor and the resulting reducing conditions lead to the simultaneous presence of metal atoms at different oxidation states, whose relative amount depends on the reaction time. Colored arrows indicate the phases found at different reaction times (green, red, blue and yellow correspond to 10, 25, 45 and 300 minutes, respectively).

different syntheses were carried out following the procedure described in the Experimental method section, changing only the dwelling time at reflux. The XRD patterns (Fig. 10) showed the formation, after 10 minutes at 370 °C, of three species: a ferrite (denoted as * in the figure) with lattice parameter a = 0.840 nm, cobalt–iron monoxide ($, $Co_{1-x}Fe_xO$) with a very low content of iron (a = 0.427(1) nm) and *fcc* $Co^{(0)}$ (#). The $Co_{1-x}Fe_xO$ disappeared after 25 minutes of reaction, the only phase observed being metal *fcc* cobalt and a spinel ferrite. On increasing the time at 370 °C up to 45 minutes a decrease of the lattice parameter value of ferrite (a = 0.837 nm) suggested the increase of cobalt content in the spinel lattice, while the crystal structure of $Co^{(0)}$ evolved from cubic to hexagonal (*hcp*, +) and a small amount of cobalt–iron alloy formed (o). When the reaction time was further increased up to 300 minutes, only reduced species appeared, according to the XRD pattern, the predominant one being the Co–Fe alloy, with a minor amount of *hcp* Co.

The obtained results can be explained by considering the extreme conditions of the reaction media in terms of temperature and redox strength, which allow the total transformation of the monoxide species in metals and spinel ferrite during the first 25 minutes. We can in fact hypothesize a mechanism of reaction as that reported in Scheme 1. The first two reactions that occur in the media are the release of $Co^{(II)}$ and $Fe^{(III)}$ by the oleate (black arrows). The decomposition of oleic acid and sodium oleate, in large amount and under an inert atmosphere, leads to a high concentration of reducing species as hydrogen (H_2) and carbon monoxide (CO), which allow the partial reduction of $Fe^{(III)}$ to $Fe^{(II)}$ and the combination of cobalt and iron divalent cations to form a mixed rock-salt monoxide ($Co_{1-x}Fe_xO$) and, with other $Fe^{(III)}$ ions still available in solution, the ferrites (Fe_3O_4 or $Co_yFe_{3-y}O_4$) (red arrows). The further step is the reduction of $Co^{(II)}$ down to the metal state. This process can be activated by the mixed mono-oxide. It is indeed well known and largely reported in the literature[54–56] that cobalt monoxide plays a role as a activator in the oxidation of CO to carbon dioxide (CO_2). According to this scheme, after 10 minutes of reaction Co-rich $Co_{1-x}Fe_xO$, $Co_y^{(II)}Fe_{1-y}^{(II)}Fe_2^{(III)}O_4$ and *fcc* $Co^{(0)}$ NPs are found in the reaction medium (for TEM images and magnetic measurements see Fig. S11a in the ESI†). After 25 minutes (Fig. S11b, ESI†) the reduction of the cobalt in the monoxide is complete and *fcc* $Co^{(0)}$ starts to transform in *hcp*, which is the most thermodynamically stable Co phase at the reaction temperature (green arrows). The reduction process of $Fe^{(II)}$ to $Fe^{(0)}$ is slower than the one involving the cobalt, and the formation of the cobalt–iron alloy was observed only after 45 minutes (blue arrows). This is probably due to the lower reduction potential of $Fe^{(II)}$ under the experimental conditions adopted, which makes its reduction possible only when the initial $Co^{(II)}$ concentration has significantly reduced. The reduction process goes further on, until, after 300 minutes most of the metal precursors have transformed in the cobalt–iron alloy, with a minor amount of *hcp* Co (orange arrows).

Our experimental results unambiguously demonstrate that the presence of NaOL is essential to make the proposed reaction scheme effective. In the literature, it is reported that the partial substitution of OA with NaOL is an effective route to reduce the amount of H_2O and CO_2 in the reaction medium, released during the condensation *via* heterocyclic cleavage of OA (ketonic decarboxylation).[57,58] In our synthesis, OA and NaOL are present in the same molar ratio; thus, we cannot exclude that the ketonic decarboxylation reaction partially occurred and then water was released. The water in the mixture can interact with the $Na^{(I)}$ cation of NaOL and increase the amount of OL^- available in the reaction medium. Moreover, the carboxylate group of this oleate has a stronger affinity for the surface of the metal monoxide[53] than OA. In the thermal decomposition synthesis, metal ions from smaller NPs are usually re-dissolved to reprecipitate forming bigger particles.[59–61] In our case, the large amount of OL^- available can modify the dissolution/precipi-

tation process of the metal ions from the initial Co–Fe monoxide NPs, stabilizing the re-dissolved metal ions as organo-metallic complexes. These complexes in solution are $Co(OL)_2$ and $Fe(OL)_2$, which partially undergo the decarboxylation reaction leading to the formation of H_2, CO_2, radical alkenes and "free" metal ions.[58] The latter are more prone to reduction by the reducing species occurring in the reaction medium than metal ions enclosed in the oxide. The proposed mechanism supports the presence of NaOL as stabilizing and reducing agents, as essential for obtaining metal/ferrite NHSs by this one-pot thermal decomposition synthesis. Finally, we would like to note that the heterodimeric morphology of the final product supports the proposed mechanism.

4. Conclusions

Summarizing, we reported here a one-pot thermal decomposition synthesis for obtaining metal/ferrite NHSs with very high saturation magnetization and large remanence and coercivity. The thorough investigation of the mechanism of the proposed synthesis approach as a function of the amount of stabilizing agents, of the nature of the metal precursors and of the decomposition time, allowed us to identify the key role played by NaOL at different steps of the reaction, down to the formation of the metal/ferrite NHSs. NaOL, indeed, does not enter the reaction pathway as a stabilizing agent only, but it is fundamental for the reduction of the mixed metal precursor down to the metal state, too. Moreover, the increase of the cobalt content in the Co–Fe oleate precursor caused the evolution of the NP shape, leading to a more elongated heterodimeric architecture, and to a modification of the relative amount of metal and spinel ferrite phases. Overall, these results suggest that the control of the relative amount of metal oleates (FeCoOL and NaOL) is a simple and efficient tool for tuning the hardness of the final NHSs. As an example, here we showed how, playing with these parameters, it is possible to more than double the BH_{max} at room temperature, from 8 (NHS-1) up to 19 (NHS-3) kJ m^{-3}. This value, which is comparable to that of some commercial Strontium ferrite based magnets, can be further and consistently improved by increasing the amount of $Co^{(II)}$ ions in the spinel lattice. Finally, it is worth stressing that unlike most of the metal/spinel ferrite NHSs prepared so far, the presence of a very thin, highly crystalline, quasi-stoichiometric cobalt ferrite shell surrounding the metal makes the NHSs highly stable in the air atmosphere for a very long time, which is crucial for further technological applications. No modification of the magnetic properties of our NHSs was in fact observed over more than one year.

Author contribution

MP and CS conceived the experiment. BM synthesized the NHSs. XPS measurements were performed by BC and BM. BM, MA, CI, MP and CS recorded and analysed the XRD patterns and magnetic data. STEM, EELS and HRTEM measurements and data analysis were performed by BM, CJF, GB, RFP, AI, CM and RMI. MP, BM and CS wrote the manuscript, which was critically revised by all the authors.

Conflicts of interest

There are no conflicts to declare.

Acknowledgements

The authors thank Dr Francesca Ridi for TGA measurements and Dr Laura Chelazzi and Dr Samuele Ciattini, at CRIST laboratory (Univ. of Florence), for XRD data analysis. This work was supported by EU-H2020 AMPHIBIAN Project (no. 720853) and by European Union's Horizon 2020 research and innovation programme under grant agreement no. 823717-ESTEEM3.

References

1 W. H. Meiklejohn and C. P. Bean, *Phys. Rev.*, 1956, **102**, 1413–1414.
2 H. Zeng, J. Li, J. P. Liu, Z. L. Wang and S. Sun, *Nature*, 2002, **420**, 395–398.
3 E. F. Kneller and R. Hawig, *IEEE Trans. Magn.*, 1991, **27**, 3588–3560.
4 F. Jimenez-Villacorta and L. H. Lewis, in *Nanomagnetism*, ed. J. M. Gonzalez Estevez, One Central Press, 2014, pp. 160–189.
5 J. Sort, J. Nogués, S. Suriñach, J. S. Muñoz, M. D. Baró, E. Chappel, F. Dupont and G. Chouteau, *Appl. Phys. Lett.*, 2001, **79**, 1142–1144.
6 O. Gutfleisch, M. a. Willard, E. Brück, C. H. Chen, S. G. Sankar and J. P. Liu, *Adv. Mater.*, 2011, **23**, 821–842.
7 J. M. D. Coey, *Magnetism and Magnetic Materials*, 2010.
8 A. H. King, R. G. Eggert and K. A. Gschneidner, in *Handbook on the Physics and Chemistry of Rare Earths*, Elsevier B.V., 1st edn, 2016, vol. 50, pp. 19–46.
9 N. T. Nassar, X. Du and T. E. Graedel, *J. Ind. Ecol.*, 2015, **19**, 1044–1054.
10 P. Weiss and R. Forrer, *Ann. Phys.*, 1929, **10**, 279–372.
11 A. López-Ortega, E. Lottini, C. D. J. Fernández and C. Sangregorio, *Chem. Mater.*, 2015, **27**, 4048–4056.
12 E. Fantechi, C. Innocenti, M. Albino, E. Lottini and C. Sangregorio, *J. Magn. Magn. Mater.*, 2015, **380**, 365–371.
13 E. Fantechi, G. Campo, D. Carta, A. Corrias, C. de Julián Fernández, D. Gatteschi, C. Innocenti, F. Pineider, F. Rugi and C. Sangregorio, *J. Phys. Chem. C*, 2012, **116**, 8261–8270.
14 C. Petit and M. P. Pileni, *J. Phys. Chem. B*, 1999, **103**, 1805–1810.
15 V. F. Puntes, K. M. Krishnan and P. Alivisatos, *Appl. Phys. Lett.*, 2001, **78**, 2187–2189.
16 G. S. Chaubey, C. Barcena, N. Poudyal, C. Rong, J. Gao, S. Sun and J. P. Liu, *J. Am. Chem. Soc.*, 2007, **129**, 7214–7215.

17 B. Aslibeiki, *Ceram. Int.*, 2016, **42**, 6413–6421.
18 L. J. Zhao and Q. Jiang, *Mater. Lett.*, 2010, **64**, 677–679.
19 A. Quesada, F. Rubio-Marcos, J. F. Marco, F. J. Mompean, M. García-Hernández and J. F. Fernández, *Appl. Phys. Lett.*, 2014, **105**, 202405.
20 B. Nakhjavan, M. N. Tahir, M. Panthöfer, H. Gao, T. Gasi, V. Ksenofontov, R. Branscheid, S. Weber, U. Kolb, L. M. Schreiber and W. Tremel, *Chem. Commun.*, 2011, **47**, 8898.
21 Z. Zhou, Y. Sun, J. Shen, J. Wei, C. Yu, B. Kong, W. Liu, H. Yang, S. Yang and W. Wang, *Biomaterials*, 2014, **35**, 7470–7478.
22 L. Wu, P.-O. Jubert, D. Berman, W. Imaino, A. Nelson, H. Zhu, S. Zhang and S. Sun, *Nano Lett.*, 2014, **14**, 3395–3399.
23 J. H. Jung, S. Kim, H. Kim, J. Park and J. H. Oh, *Small*, 2015, **11**, 4976–4984.
24 E. Fantechi, C. Innocenti, M. Zanardelli, M. Fittipaldi, E. Falvo, M. Carbo, V. Shullani, L. Di Cesare Mannelli, C. Ghelardini, A. M. Ferretti, A. Ponti, C. Sangregorio and P. Ceci, *ACS Nano*, 2014, **8**, 4705–4719.
25 K. F. Ortega, S. Anke, S. Salamon, F. Özcan, J. Heese, C. Andronescu, J. Landers, H. Wende, W. Schuhmann, M. Muhler, T. Lunkenbein and M. Behrens, *Chem. – Eur. J.*, 2017, **23**, 12443–12449.
26 A. Quesada, C. Granados-Miralles, A. López-Ortega, S. Erokhin, E. Lottini, J. Pedrosa, A. Bollero, A. M. Aragón, F. Rubio-Marcos, M. Stingaciu, G. Bertoni, C. de Julián Fernández, C. Sangregorio, J. F. Fernández, D. Berkov and M. Christensen, *Adv. Electron. Mater.*, 2016, **2**, 1500365.
27 G. Cotin, C. Kiefer, F. Perton, D. Ihiawakrim, C. Blanco-Andujar, S. Moldovan, C. Lefevre, O. Ersen, B. Pichon, D. Mertz and S. Bégin-Colin, *Nanomaterials*, 2018, **8**, 881.
28 W. Baaziz, B. P. Pichon, J.-M. Grenèche and S. Begin-Colin, *CrystEngComm*, 2018, **20**, 7206–7220.
29 D. A. Shirley, *Phys. Rev. B: Solid State*, 1972, **5**, 4709–4714.
30 G. Bertoni and J. Verbeeck, *Ultramicroscopy*, 2008, **108**, 782–790.
31 M. C. Biesinger, L. W. M. Lau, A. R. Gerson and R. S. C. Smart, *Appl. Surf. Sci.*, 2010, **257**, 887–898.
32 W. P. Wang, H. Yang, T. Xian and J. L. Jiang, *Mater. Trans.*, 2012, **53**, 1586–1589.
33 D. Wilson and M. A. Langell, *Appl. Surf. Sci.*, 2014, **303**, 6–13.
34 T. Aghavnian, J. B. Moussy, D. Stanescu, R. Belkhou, N. Jedrecy, P. Ohresser, H. Magnan, M.-A. Arrio, Ph. Sainctavit and A. Barbier, *J. Electron Spectrosc. Relat. Phenom.*, 2016, **202**, 16–21.
35 E. J. W. Verwey, *Nature*, 1939, **144**, 327–328.
36 J. Abellan and M. Ortuno, *Phys. Status Solidi*, 1986, **96**, 581–586.
37 T. Orlando, S. Mannucci, E. Fantechi, G. Conti, S. Tambalo, A. Busato, C. Innocenti, L. Ghin, R. Bassi, P. Arosio, F. Orsini, C. Sangregorio, M. Corti, M. F. Casula, P. Marzola, A. Lascialfari and A. Sbarbati, *Contrast Media Mol. Imaging*, 2016, **11**, 139–145.
38 B. K. Pugh, D. P. Kramer and C. H. Chen, *IEEE Trans. Magn.*, 2011, **47**, 4100–4103.
39 Y. Bao and K. M. Krishnan, *J. Magn. Magn. Mater.*, 2005, **293**, 15–19.
40 G. Asti, M. Ghidini, R. Pellicelli, C. Pernechele, M. Solzi, F. Albertini, F. Casoli, S. Fabbrici and L. Pareti, *Phys. Rev. B: Condens. Matter Mater. Phys.*, 2006, **73**, 094406.
41 M. Ghidini, G. Asti, R. Pellicelli, C. Pernechele and M. Solzi, *J. Magn. Magn. Mater.*, 2007, **316**, 159–165.
42 F. E. Luborsky and T. O. Paine, *J. Appl. Phys.*, 1960, **31**, S68–S70.
43 G. C. P. Leite, E. F. Chagas, R. Pereira, R. J. Prado, A. J. Terezo, M. Alzamora and E. Baggio-Saitovitch, *J. Magn. Magn. Mater.*, 2012, **324**, 2711–2716.
44 Y. Kumar, A. Sharma, M. A. Ahmed, S. S. Mali, C. K. Hong and P. M. Shirage, *New J. Chem.*, 2018, **42**, 15793–15802.
45 C. Dobbrow and A. M. Schmidt, *Beilstein J. Nanotechnol.*, 2012, **3**, 75–81.
46 C. J. Chen, R. K. Chiang, S. Kamali and S. L. Wang, *Nanoscale*, 2015, **7**, 14332–14343.
47 C. Moya, G. Salas, M. del P. Morales, X. Batlle and A. Labarta, *J. Mater. Chem. C*, 2015, **3**, 4522–4529.
48 W. Baaziz, B. P. Pichon, Y. Liu, J. M. Grenèche, C. Ulhaq-Bouillet, E. Terrier, N. Bergeard, V. Halté, C. Boeglin, F. Choueikani, M. Toumi, T. Mhiri and S. Begin-Colin, *Chem. Mater.*, 2014, **26**, 5063–5073.
49 N. Bao, L. Shen, Y. Wang, P. Padhan and A. Gupta, *J. Am. Chem. Soc.*, 2007, **129**, 12374–12375.
50 E. Lottini, A. López-Ortega, G. Bertoni, S. Turner, M. Meledina, G. Van Tendeloo, C. de Julián Fernández and C. Sangregorio, *Chem. Mater.*, 2016, **28**, 4214–4222.
51 M. V. Kovalenko, M. I. Bodnarchuk, R. T. Lechner, G. Hesser, F. Schäffler and W. Heiss, *J. Am. Chem. Soc.*, 2007, **129**, 6352–6353.
52 L. Wang and L. Gao, *J. Phys. Chem. C*, 2009, 15914–15920.
53 Z. Zhou, X. Zhu, D. Wu, Q. Chen, D. Huang, C. Sun, J. Xin, K. Ni and J. Gao, *Chem. Mater.*, 2015, **27**, 3505–3515.
54 M. Kang, *Appl. Catal., A*, 2003, **251**, 143–156.
55 C.-B. Wang, C.-W. Tang, H.-C. Tsai and S.-H. Chien, *Catal. Lett.*, 2006, **107**, 223–230.
56 P. Thormählen, M. Skoglundh, E. Fridell and B. Andersson, *J. Catal.*, 1999, **188**, 300–310.
57 J. Muro-Cruces, A. G. Roca, A. López-Ortega, E. Fantechi, D. Del-Pozo-Bueno, S. Estradé, F. Peiró, B. Sepúlveda, F. Pineider, C. Sangregorio and J. Nogues, *ACS Nano*, 2019, **13**, 7716–7728.
58 S. J. Kemp, R. M. Ferguson, A. P. Khandhar and K. M. Krishnan, *RSC Adv.*, 2016, **6**, 77452–77464.
59 N. Pinna and M. Kamaoui, *Advanced Wet-Chemical Synthetic Approaches to Inorganic Nanostructures*, 2008.
60 T. Sugimoto, *Monodispersed Particles*, 2001.
61 J. Park, J. Joo, S. G. Kwon, Y. Jang and T. Hyeon, *Angew. Chem., Int. Ed.*, 2007, **46**, 4630–4660.